

Ultrasmall spot size scanning laser ophthalmoscopy

Brian Vohnsen* and Diego Rativa

Advanced Optical Imaging Group, School of Physics, University College Dublin, Dublin 4, Ireland
*brian.vohnsen@ucd.ie

Abstract: An ultrasmall spot size scanning laser ophthalmoscope has been developed that employs an annular aberration-corrected incident beam to increase the effective numerical aperture of the eye thereby reducing the width of the probing light spot. Parafovea and foveal cone photoreceptor visibility determined from small area retinal image scans are discussed from the perspective of mode matching between the focused incident beam and the waveguide modes of individual cones. The cone visibility near the fovea centralis can be increased with the annular illumination scheme whereas the visibility of larger parafovea cones drops significantly as a consequence of poorer mode match. With further improvements of the implemented wavefront correction technology it holds promise for individual cone-photoreceptor imaging at the fovea centralis and for optical targeting of the retina with increased resolution.

©2011 Optical Society of America

OCIS codes: (170.0110) Imaging systems; (170.5755) Retina scanning; (330.5310) Vision—photoreceptors; (330.7327) Visual optics, ophthalmic instrumentation

References and links

1. R. H. Webb, G. W. Hughes, and O. Pomerantzoff, "Flying spot TV ophthalmoscope," *Appl. Opt.* **19**(17), 2991–2997 (1980).
2. B. Vohnsen, I. Iglesias, and P. Artal, "Directional imaging of the retinal cone mosaic," *Opt. Lett.* **29**(9), 968–970 (2004).
3. A. Roorda, F. Romero-Borja, W. Donnelly Iii, H. Queener, T. J. Hebert, and M. C. W. Campbell, "Adaptive optics scanning laser ophthalmoscopy," *Opt. Express* **10**(9), 405–412 (2002).
4. Y. Zhang and A. Roorda, "Evaluating the lateral resolution of the adaptive optics scanning laser ophthalmoscope," *J. Biomed. Opt.* **11**(1), 014002 (2006).
5. R. D. Ferguson, Z. Zhong, D. X. Hammer, M. Mujat, A. H. Patel, C. Deng, W. Zou, and S. A. Burns, "Adaptive optics scanning laser ophthalmoscope with integrated wide-field retinal imaging and tracking," *J. Opt. Soc. Am. A* **27**(11), A265–A277 (2010).
6. K. Y. Li, P. Tiruveedhula, and A. Roorda, "Intersubject variability of foveal cone photoreceptor density in relation to eye length," *Invest. Ophthalmol. Vis. Sci.* **51**(12), 6858–6867 (2010).
7. E. A. Rossi, M. Chung, A. Dubra, J. J. Hunter, W. H. Merigan, and D. R. Williams, "Imaging retinal mosaics in the living eye," *Eye (Lond.)* **25**(3), 301–308 (2011).
8. J. M. Enoch, "Optical properties of the retinal receptors," *J. Opt. Soc. Am.* **53**(1), 71–85 (1963).
9. B. Vohnsen, I. Iglesias, and P. Artal, "Guided light and diffraction model of human-eye photoreceptors," *J. Opt. Soc. Am. A* **22**(11), 2318–2328 (2005).
10. P. J. Delint, T. T. J. M. Berendschot, and D. van Norren, "Local photoreceptor alignment measured with a scanning laser ophthalmoscope," *Vision Res.* **37**(2), 243–248 (1997).
11. A. Roorda and D. R. Williams, "Optical fiber properties of individual human cones," *J. Vis.* **2**(5), 4 (2002).
12. B. Vohnsen, "Photoreceptor waveguides and effective retinal image quality," *J. Opt. Soc. Am. A* **24**(3), 597–607 (2007).
13. B. Vohnsen and D. Rativa, "Absence of an integrated Stiles-Crawford function for coherent light," *J. Vis.* **11**(1), 19 (2011).
14. B. Vohnsen, I. Iglesias, and P. Artal, "Directional light scanning laser ophthalmoscope," *J. Opt. Soc. Am. A* **22**(12), 2606–2612 (2005).
15. Q. V. Hoang, R. A. Linsenmeier, C. K. Chung, and C. A. Curcio, "Photoreceptor inner segments in monkey and human retina: mitochondrial density, optics, and regional variation," *Vis. Neurosci.* **19**(04), 395–407 (2002).
16. W. Gao, B. Cense, Y. Zhang, R. S. Jonnal, and D. T. Miller, "Measuring retinal contributions to the optical Stiles-Crawford effect with optical coherence tomography," *Opt. Express* **16**(9), 6486–6501 (2008).
17. A. Pallikaris, D. R. Williams, and H. Hofer, "The reflectance of single cones in the living human eye," *Invest. Ophthalmol. Vis. Sci.* **44**(10), 4580–4592 (2003).

18. R. S. Jonnal, J. R. Besecker, J. C. Derby, O. P. Kocaoglu, B. Cense, W. Gao, Q. Wang, and D. T. Miller, "Imaging outer segment renewal in living human cone photoreceptors," *Opt. Express* **18**(5), 5257–5270 (2010).
19. M. Pircher, J. S. Kroisamer, F. Felberer, H. Sattmann, E. Götzinger, and C. K. Hitzenberger, "Temporal changes of human cone photoreceptors observed *in vivo* with SLO/OCT," *Biomed. Opt. Express* **2**(1), 100–112 (2011).
20. G. Toraldo di Francia, "Retina cones as dielectric antennas," *J. Opt. Soc. Am.* **39**(4), 324 (1949).
21. T. Y. P. Chui, H. Song, and S. A. Burns, "Adaptive-optics imaging of human cone photoreceptor distribution," *J. Opt. Soc. Am. A* **25**(12), 3021–3029 (2008).
22. N. M. Putnam, D. X. Hammer, Y. Zhang, D. Merino, and A. Roorda, "Modeling the foveal cone mosaic imaged with adaptive optics scanning laser ophthalmoscopy," *Opt. Express* **18**(24), 24902–24916 (2010).
23. E. J. Fernández, B. Hermann, B. Považay, A. Unterhuber, H. Sattmann, B. Hofer, P. K. Ahnelt, and W. Drexler, "Ultrahigh resolution optical coherence tomography and pano-correction for cellular imaging of the living human retina," *Opt. Express* **16**(15), 11083–11094 (2008).
24. R. J. Zawadzki, B. Cense, Y. Zhang, S. S. Choi, D. T. Miller, and J. S. Werner, "Ultrahigh-resolution optical coherence tomography with monochromatic and chromatic aberration correction," *Opt. Express* **16**(11), 8126–8143 (2008).
25. N. M. Putnam, H. J. Hofer, N. Doble, L. Chen, J. Carroll, and D. R. Williams, "The locus of fixation and the foveal cone mosaic," *J. Vis.* **5**(7), 3 (2005).
26. M. Born and E. Wolf, "Principles of Optics," 6th Edition (Pergamon Press, Oxford) p. 416 (1991).
27. C. J. R. Sheppard and A. Choudhury, "Image formation in the scanning microscope," *Opt. Acta (Lond.)* **24**, 1051–1073 (1977).
28. G. J. Brakenhoff, P. Blom, and P. Barends, "Confocal scanning light microscopy with high aperture immersion lenses," *J. Microsc. (Oxford)* **117**, 219–232 (1979).
29. T. Wilson and S. J. Hewlett, "The use of annular pupil plane filters to tune the imaging properties in confocal microscopy," *J. Mod. Opt.* **37**(12), 2025–2046 (1990).
30. E. H. Linfoot and E. Wolf, "Diffraction images in systems with an annular aperture," *Proc. Phys. Soc. B* **66**(2), 145–149 (1953).
31. W. T. Welford, "Use of annular apertures to increase focal depth," *J. Opt. Soc. Am.* **50**(8), 749–753 (1960).
32. S. W. Hell, P. E. Hänninen, A. Kuusisto, M. Schrader, and E. Soini, "Annular aperture two-photon excitation microscopy," *Opt. Commun.* **117**(1-2), 20–24 (1995).
33. C. J. R. Sheppard and A. Choudhury, "Annular pupils, radial polarization, and superresolution," *Appl. Opt.* **43**(22), 4322–4327 (2004).
34. G. Toraldo di Francia, "Super-gain antennas and optical resolving power," *Nuovo Cim.* **9**(S3 Suppl.), 426–438 (1952).
35. D. Rativa and B. Vohnsen, "Analysis of individual cone-photoreceptor directionality using scanning laser ophthalmoscopy," *Biomed. Opt. Express* **2**(6), 1423–1431 (2011).
36. D. W. Arathorn, Q. Yang, C. R. Vogel, Y. Zhang, P. Tiruveedhula, and A. Roorda, "Retinally stabilized cone-targeted stimulus delivery," *Opt. Express* **15**(21), 13731–13744 (2007).
37. N. Doble, S. S. Choi, J. L. Codona, J. Christou, J. M. Enoch, and D. R. Williams, "In vivo imaging of the human rod photoreceptor mosaic," *Opt. Lett.* **36**(1), 31–33 (2011).
38. R. Seth and P. Gouras, "Assessing macular pigment from SLO images," *Doc. Ophthalmol.* **108**(3), 197–202 (2004).
39. O. P. Kocaoglu, S. Lee, R. S. Jonnal, Q. Wang, A. E. Herde, J. C. Derby, W. Gao, and D. T. Miller, "Imaging cone photoreceptors in three dimensions and in time using ultrahigh resolution optical coherence tomography with adaptive optics," *Biomed. Opt. Express* **2**(4), 748–763 (2011).
40. L. C. Sincich, Y. Zhang, P. Tiruveedhula, J. C. Horton, and A. Roorda, "Resolving single cone inputs to visual receptive fields," *Nat. Neurosci.* **12**(8), 967–969 (2009).
41. D. Rativa and B. Vohnsen, "Simulating human photoreceptor optics using a liquid-filled photonic crystal fiber," *Biomed. Opt. Express* **2**(3), 543–551 (2011).
42. E. Zrenner, K. U. Bartz-Schmidt, H. Benav, D. Besch, A. Bruckmann, V.-P. Gabel, F. Gekeler, U. Greppmaier, A. Harscher, S. Kibbel, J. Koch, A. Kusnyerik, T. Peters, K. Stingl, H. Sachs, A. Stett, P. Szurman, B. Wilhelm, and R. Wilke, "Subretinal electronic chips allow blind patients to read letters and combine them to words," *Proc. Biol. Sci.* **278**(1711), 1489–1497 (2011).

1. Introduction

Scanning laser ophthalmoscopes (SLO's) commonly make use of a narrow incident beam of light that when focused by the optics of the eye is raster scanned to image the retina [1]. To resolve individual cone photoreceptors in the human eye with an SLO a wider incident beam and confocal detection is needed [2] often in combination with wavefront correction that compensate eye and system aberrations [3–7].

It has been demonstrated that cone photoreceptors can guide light with modes that resemble those of cylindrical dielectric waveguides [8], and indeed waveguiding is central for the interpretation of the directional light-capture efficiency of cones recognized in the Stiles-Crawford effects of visual optics [9]. To ensure that the cones appear as bright as possible in retinal images it is essential that the focused scanning beam is incident along the

photoreceptor axes with a minimum of aberrations thereby increasing the light-coupling efficiency [2,10–14]. Cones appear bright in retinal images predominantly due to backscattering from the elevated refractive index of mitochondria located at the ellipsoid transition from inner- to outer segments [15,16] although temporal and outer-segment changes can also affect their visibility [17–19]. Cone photoreceptor alignment with respect to the incident illumination has previously been studied with SLO [2,10] and with flood illumination fundus photography [11]. The individual cone photoreceptors can be consistently resolved with an SLO provided that the scanning spot is comparable to or smaller than the cone diameter (and spacing) and that a small confocal pinhole is used to prevent unwanted stray light from masking the imaged cones [14]. Thus, in the waveguide picture of cones, it becomes a task of optimizing the radiative transfer and coupling efficiency of incident radiation to permitted modes of the retina receptors [9,20].

Generally, it remains a challenge to resolve the cones at the fovea centralis with an SLO [21,22] (as well as with Optical Coherence Tomography (OCT) [23,24]) owing to the smallness of the foveal receptors and their dense packing arrangement. Flood illumination techniques employing adaptive optics have typically been more successful than scanning techniques to resolve the foveal cone mosaic using incoherent short (few milliseconds) flashes of green light thereby eliminating interference and motion artifacts [7,25]. Few successful SLO designs (using typically red or near-IR light) have obtained comparable resolution to revolve the cone mosaic at or very near the fovea, and indeed only recently have the first high-quality SLO fovea cone-mosaic images been reported [6,7]. To resolve fovea cones, the scanning beam should be focused to a spot diameter in the range of 2.0 to 2.5 μm , and even if accomplished the reflectivity of the fovea cones might be too low to appear clearly in recorded images. For the larger parafovea cones with diameters that exceed 5 μm a suitable spot size is easier to achieve. To reduce the spot size a shorter wavelength (where absorption and scattering as well as comfort and safety may be limiting factors), a larger pupil with increased aberrations, or an annular beam profile that effectively increases the numerical aperture of the eye may be used. In this work the latter approach is explored using a central stop to create an annular beam that decreases the scanning spot size [26] as required for cone imaging at or near the fovea centralis. Annular apertures have been used in confocal microscopy to narrow the central PSF [27–29] and increase the depth of focus [30,31] of relevance also in two-photon microscopy [32]. High NA objectives need special attention because of the vectorial properties of light [33] whereas a scalar analysis suffices for the eye.

This paper is organized as follows: Section 2 contains a description of the system layout and the expectations regarding the annular illumination scheme, Section 3 contains experimental results for parafovea regions and the fovea centralis, the results are discussed in Section 4, and in Section 5 we offer our conclusions.

2. Experimental setup and annular-illumination concept

2.1 Experimental realization

A schematic drawing of the system is shown in Fig. 1. A set of annular apertures made with a vapor-deposited aluminum coating on a microscope glass slide is used to create an annular beam that is projected onto the eye pupil. The annuli allow a central beam stop which at the eye equals 1 to 4 mm in steps of 1 mm with the outer beam diameter fixed at 5 mm. An expanded ($\sim\!10$ mm) collimated NIR laser diode (785 nm) is used as source with illumination compensation made for each annulus to maintain a constant incident power at the eye. Images with adjustable viewing angle are collected at 47 fps using a set of galvanometric scanners one of which is a 12 kHz resonant scanner. The SLO has been designed with reflective optics to prevent unwanted system reflections. A Hartmann-Shack (HS) wavefront sensor is used together with a Boston Micromachines 140-actuator deformable mirror and a Badal defocus adjustment to compensate aberrations of the wavefront incident and reflected from the eye fundus. To minimize beam alignment inaccuracies on the deformable mirror a CCD camera is used for improved visualization of the beam path prior to retinal imaging (not

shown in Fig. 1). The signal is measured with an avalanche photodiode (APD) in a confocal setup where a pinhole is used to eliminate stray light. It should be noted that the annulus is used only in the incident path to generate the annular beam whereas light reflected by the eye fundus is limited only by the unobstructed size of the eye pupil. To facilitate imaging, the accommodation has been paralyzed and the pupil dilated by administrating 2 drops of 1% tropicamide followed by another drop every 2 hours during image acquisition sessions. A distant green LED is used as fixation target to reduce unwanted eye motion during acquisitions. The study has been approved by the UCD Human Research Ethics Committee and is complying with the Declaration of Helsinki for research involving human subjects.

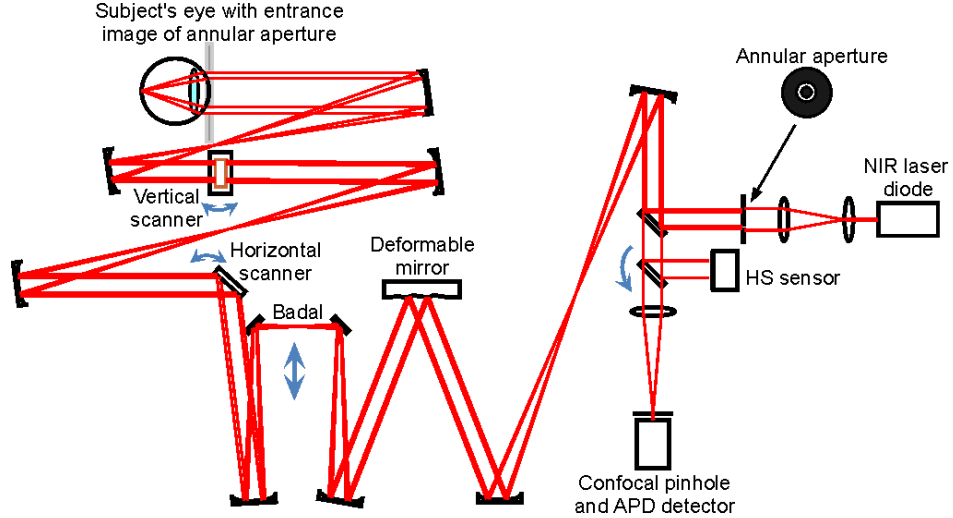


Fig. 1. Schematic layout of the annular illumination confocal SLO with adaptive optics for wavefront correction of the eye and system. The wavefront is sensed in the backward direction with a dilated unrestricted pupil whereas in the entrance path an annular aperture restricts the profile of the beam incident on the eye to an annulus of 5 mm outer diameter.

Ocular wavefront correction for a given retinal position is made with the scanners stopped in their neutral position using the Badal for defocus correction and, following, the deformable mirror in a closed-loop correction (previously calibrated with the same laser). Only when a satisfactory correction has been obtained across the 5 mm pupil (based on the condition that the remnant RMS wavefront error is on the order of $\lambda/4$ or less) are the scanners reactivated, the illumination power increased and a motorized flip mirror switched to change the detection light path from the HS sensor to the APD. We expect that the remnant wavefront aberration may be additionally reduced with further system optimization in continuation of this work. In addition to the wavefront, the improved correction is also verified by the subject (when not scanning) and by the improvement in obtainable image quality. The power incident on the eye is 50 μW during the closed-loop wavefront correction with a static beam and 1.0 mW during the imaging in compliance with the ANSI safety standard Z136.1 for small extended sources during a typical video acquisition time of 2 seconds.

2.2 Theoretical expectations with an annular illumination scheme

The annular illumination concept is illustrated in Fig. 2(a) where theoretical diffraction-limited PSF's for a full and an annular 5 mm pupil are shown incident on an array of cone photoreceptors. The coupling to the central cone is illustrated by a quasi-Gaussian mode [9] in the inner segment and partial backscattering by the ellipsoid and the outer segment. This backscattered light allows imaging of the cones and its directionality has formerly been evaluated using OCT allowing a determination of the contributions resulting from both the inner-outer segment junction and the posterior part of the outer segments [16].

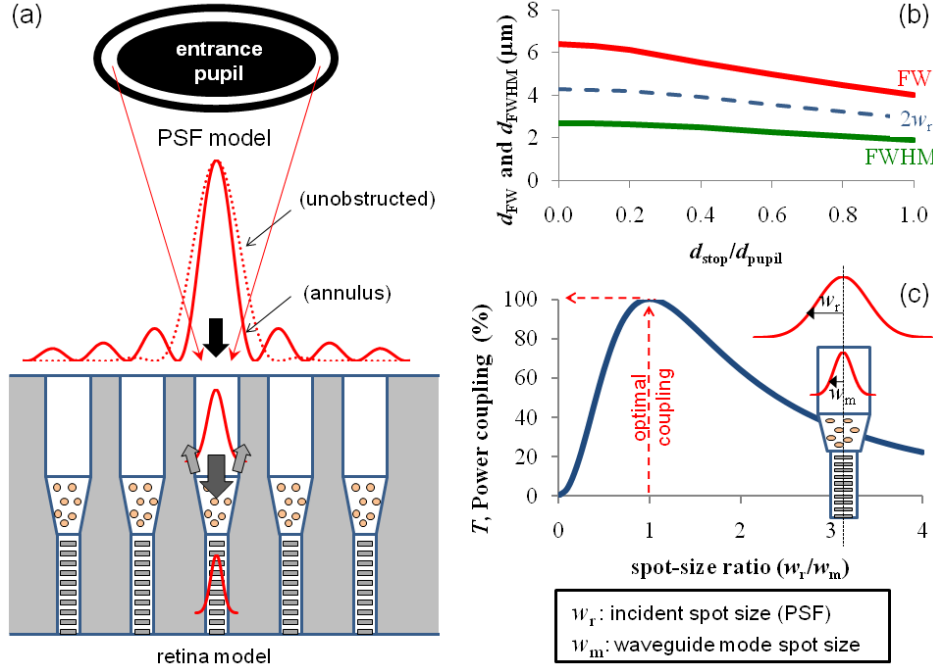


Fig. 2. Theoretical analysis of the PSF attainable with annular illumination in terms of (a) PSF focal spot size with and without the central obstruction schematically coupled to the fundamental mode of a central waveguide cone; (b) FW and FWHM for the central Airy disc as a function of the size of the circular beam obstruction for a schematic eye with $f_{\text{eye}} = 22.2$ mm and $n_{\text{eye}} = 1.33$, $d_{\text{pupil}} = 5$ mm outer-beam diameter, and adjustable stop diameter d_{stop} . For convenience also the equivalent PSF spot diameter $2w_r$ for a Gaussian beam has been shown (dashed line); (c) Theoretical power-coupling efficiency, T , when the incident PSF is assumed to be Gaussian with a spot size of w_r and the cone waveguide to which light is coupled is specified by a Gaussian mode with spot size w_m . The mode matching is illustrated for a schematic cone and an incident Gaussian-like PSF.

The annular illumination gives rise to an increased off-axis intensity ringing but in turn the Airy disc is substantially narrowed and therefore better matched to smaller cones. The full width (FW) of the Airy disc of the PSF can in the paraxial limit be calculated from

$$d_{\text{FW}} = \alpha \frac{\lambda}{NA} \quad (1)$$

where $\alpha = 1.220$ for an unobstructed pupil, and the numerical aperture of a schematic eye with focal length f_{eye} and refractive index n_{eye} is $NA = (d_{\text{pupil}} n_{\text{eye}})/(2f_{\text{eye}})$ where the incident beam diameter is d_{pupil} . When the centre of the incident beam is blocked across a diameter d_{stop} ($< d_{\text{pupil}}$) the parameter α decreases towards a lower limit $\alpha \rightarrow 0.765$ or equally 62.7% of the spot size attainable with an unobstructed pupil [26]. Thus, an effective numerical aperture of the eye for an annular beam, NA^* , may be expressed in terms of the NA of the unobstructed eye as

$$NA^* = \frac{1.22}{\alpha} NA \rightarrow 1.59 NA. \quad (2)$$

When the diameter of the central beam stop is increased, the width of the Airy disc decreases. This is shown in Fig. 2(b) for the FW and full-width-at-half-maximum (FWHM) for a 5 mm beam as a function of blockage $d_{\text{stop}}/d_{\text{pupil}}$ from 0 to 100%. In consequence, a narrow 5 mm annulus is capable of producing a spot size comparable to that of a $5 \times 1.59 = 8$ mm diffraction-limited full pupil, i.e., 1.9 μm at FWHM (4.0 μm FW) at the 785 nm

illumination wavelength. Likewise, an 8 mm annulus has the potential to focus light to a spot size comparable to that of a (fictitious) 13 mm full pupil. The reduction in spot size is, however, accompanied by a drop in the central peak power as well as an increased off-axis intensity ringing that may impact on neighboring photoreceptors. This ringing is filtered in the images by the confocal pinhole, if chosen to match the central Airy disc, and could potentially be reduced using annular Toraldo phase filters [34]. To retain sufficient power in the central spot, we have chosen to restrict the diameter of the obstruction to an 80% maximum of the beam (i.e., an annulus with 4 mm inner and 5 mm outer diameter).

The fraction of axially-incident light power that couples to any given cone, T , can be estimated using a Gaussian approximation for both the incident PSF (spot size: w_r) and for the fundamental waveguide mode (spot size: w_m) resulting in the following relation [9]

$$T = \left(\frac{2w_r / w_m}{(w_r / w_m)^2 + 1} \right)^2 \quad (3)$$

where $T = 1$ corresponds to a perfect match, i.e., $w_r = w_m$. The case of flood illumination (or a wide incident beam) may also be considered from Eq. (3) resulting in $T = 4(w_m/w_r)^2$. The focal spot diameter ($2w_r$) for a Gaussian PSF approximation equals approximately $0.7 \times \text{FW}$ of the Airy disc expressed in Eq. (1) and is indicated with a dashed line in Fig. 2(b). The diffraction-limited spot diameter obtainable with different annuli for the 785 nm wavelength is summarized in Table 1. The exact mode-width diameter $2w_m$ of photoreceptor cones is unknown but it is generally slightly larger (typically up to about 30%) than the geometrical cone diameter, d_{cone} , as determined by the V -parameter of the waveguide, i.e., $V = (\pi d_{\text{cone}}/\lambda)NA_{\text{cone}}$ (being dependent on the diameter, the numerical aperture of the cone NA_{cone} , and wavelength) [9,35]. From Table 1 can be seen that the ideal match for a cone diameter of only 2 μm would imply an 8 mm pupil with a central blockage in the range of 40 to 80% at the chosen wavelength.

Table 1. Predicted PSF Gaussian spot diameter $2w_r$ with different blockage of a 5 and 8 mm pupil

$d_{\text{stop}}/d_{\text{pupil}}$	0%	20%	40%	60%	80%	$\rightarrow 100\%$
$2w_r^*$ (μm)	4.31	4.20	3.92	3.57	3.24	2.92
$2w_r^†$ (μm)	2.70	2.62	2.45	2.24	2.02	1.83

*With a 5 mm pupil.

†With an 8 mm pupil.

Oblique incidence of light as in the Stiles-Crawford effect [2,16,35] or scanning off-axis a cone waveguide reduces the coupling efficiency (although it may impact on neighboring photoreceptors). This more general case has been considered in Ref [9]. Defocus may also impact the coupling efficiency although the beam may be considered as being in focus for a depth determined by twice the Rayleigh length conveniently written as $2Z_R = (\pi n_{\text{eye}}/2\lambda)(2w_r)^2$. The depth-of-focus increases additionally for the case of an annular illumination [30,31]. Equation (3) implies that if the spot size of the focused beam is either $2 \times$ or $0.5 \times$ that of the perfect match then the predicted power coupling drops by 36%. Likewise, a mismatch of $4 \times$ or $0.25 \times$ corresponds to a drop of 78%. Equation (3) is shown in Fig. 2(c) as a function of the spot-size ratio. Clearly, it is an idealization for “perfect” single-mode cylindrical waveguides but nonetheless it highlights the importance of matching the incident illumination to the size of the cones being imaged for maximized light coupling and photoreceptor contrast from backscattered light. Actually, while only a few modes are allowed [8] axially-incident light would predominantly couple to the fundamental mode [9]. In the case of highly multimode waveguides (presumably the large parafovea cones) optimized coupling becomes an issue of restricting the incident illumination to the acceptance angle (and thus NA) of the cones. Adaptive optics has already proven its effectiveness when imaging parafovea cones with an SLO [3–6,21,22] but it is likely that the mode-matching concept may be utilized to optimize imaging of fovea cones where adaptive optics may not fully suffice at infrared wavelengths

(dependent on the beam diameter). Increasing the NA by making use of an even wider incident beam could be an option, and indeed successful fovea imaging has been realized with such optimized systems [6,7], but it could increase the demands for stroke of the deformable mirror. The increase of the effective NA^* as indicated by Eq. (2) appears to be an attractive option to tune even the best adaptive optics scanning retinal imaging systems towards an improved performance in terms of resolution and photoreceptor contrast.

Figure 3 shows an experimental verification of the magnified PSF recorded in the actual SLO using annular apertures of fixed 5 mm outer diameter with the set of central beam stops ranging from 1 to 4 mm in the plane of the eye pupil. In the case of a diffraction-limited schematic eye this corresponds to $NA^* = 1.00 \times NA$ (no annulus), $NA^* = 1.05 \times NA$ (annulus 1), $NA^* = 1.15 \times NA$ (annulus 2), $NA^* = 1.28 \times NA$ (annulus 3), and up to $NA^* = 1.43 \times NA$ (annulus 4). The decrease of the Airy disc once the central beam stop is increased is apparent although despite of the adaptive optics wavefront correction the resulting PSF remains slightly worse than diffraction limited (the remnant RMS wavefront error was $\sim 0.08 \mu\text{m}$ across the 5 mm pupil). For annulus 4 the Airy disc is about 4 pixels wide on the CCD that with the $6 \times$ magnification telescope used corresponds to approximately $2.1 \mu\text{m}$ if accomplished in the eye.

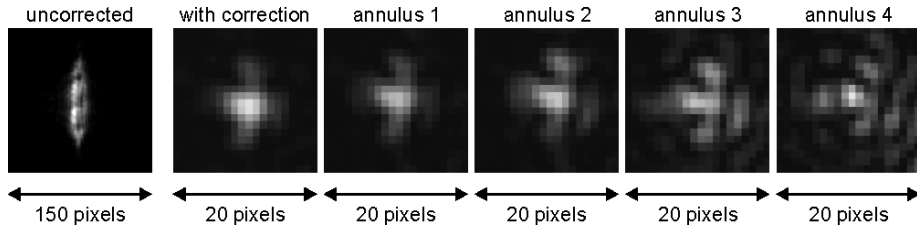


Fig. 3. Experimental verification of the PSF recorded in the actual system using a 5 mm beam without and with wavefront correction and with the use of annular illumination of increasing central blockage from 1 to 4 mm. A $6 \times$ magnification telescope together with an $f = 25 \text{ mm}$ achromatic lens and a CCD (pixel size $4.7 \mu\text{m}$) was inserted in place of the eye to record the experimental PSF. The most significant improvement was obtained with the adaptive optics correction of predominantly system astigmatism (uncorrected RMS wavefront error was $\sim 0.58 \mu\text{m}$) but the Airy disc narrowed further with the increase of the effective NA^* . Note the different scale of the PSF images prior to and after wavefront correction.

3. Experimental results

The parafovea and fovea regions for the right eye of subject BV (41 years; normal vision) have been examined with the annular illumination scheme and results obtained are shown in this section. In each case the illumination was adjusted to compensate for the shadowing caused by the beam blockage to keep a constant incident power on the eye. Images and videos represent unprocessed raw data with the exception of having corrected frames for the harmonic motion of the horizontal resonant scanner and brightness adjusted to compensate for the power reduction in the Airy disc with increased central beam blockage (assuming a diffraction-limited correction that although not obtained would be the ideal aim).

A confocal $75 \mu\text{m}$ pinhole (corresponding to $6 \mu\text{m}$ if projected onto the retina and thus comparable to the individual parafoveal cone diameter) was used for the recordings. This pinhole size does not suffice to resolve reliably the individual foveal cones but it does effectively mask the interference ringing from annulus 1 and 2 while not entirely for annulus 3 and 4 as can be seen from Fig. 2(b). In the absence of the annulus the Airy disc contains 84% of the total power (as compared to only 7% in the first interference ring). However, for annulus 4 only 17% of the total power is retained in the Airy disc while 33% of the power is contained in the first interference ring that does, however, spread over a larger area (see Fig. 3). To benefit fully from the resolution enhancement offered by annulus 3 and 4 a smaller confocal pinhole would be required. No noise reduction or de-convolution techniques have been used on the individual image frames. In each video a fixed reference point has been selected and frames have been cross-correlated to reduce unwanted motion in the playback [36]. All videos have been shortened to typically 0.5 seconds so as to limit degradation caused

by ocular saccades that may require implementation of fast eye tracking for improved video visualization [5].

3.1 Superior parafovea retina at 10 degrees

Video sequences adjusted for maximum photoreceptor visibility have been recorded for the superior parafovea retina at 10° viewing angle results of which are shown in Fig. 4. Despite of having the same power entering the eye, the visibility of cones drops significantly for the annular beam as expected on account of the reduced power-coupling efficiency predicted by Eq. (3) in the limit of $w_r \ll w_m$ although derived for single-mode waveguides. I.e., less light is contained within the acceptance angle of the (presumably multimode) cones. As a consequence, larger cones are washed out from the images once the scanning light spot from the annular beam is focused tightly. It is tempting to apply this approach to reduce the brightness of large cones whereby smaller features including rods may become easier to identify [37] provided that their reflectivity is large enough for visualization above the background noise. However, since the average pixel size in Fig. 4 is about 0.5 μm it remains highly challenging to identify structures as small as the individual rods at this scale. A reduced size of the structures is apparent once the annulus is used but this may also be a consequence of the convolution with the smaller incident PSF during scanning.

The influence of mode match may also be appreciated by the fact that the uncorrected beam (with the wider PSF) appears better coupled to the cones whereas the wavefront correction actually reduces the contrast and quality of the recorded images when no annulus is used. An impact of defocus cannot entirely be excluded although for the wavefront-corrected unobstructed beam the predicted depth of focus ($2Z_R$) is approximately 50 μm and thus comparable to the inner segment length. With the annular beam created by a central stop only

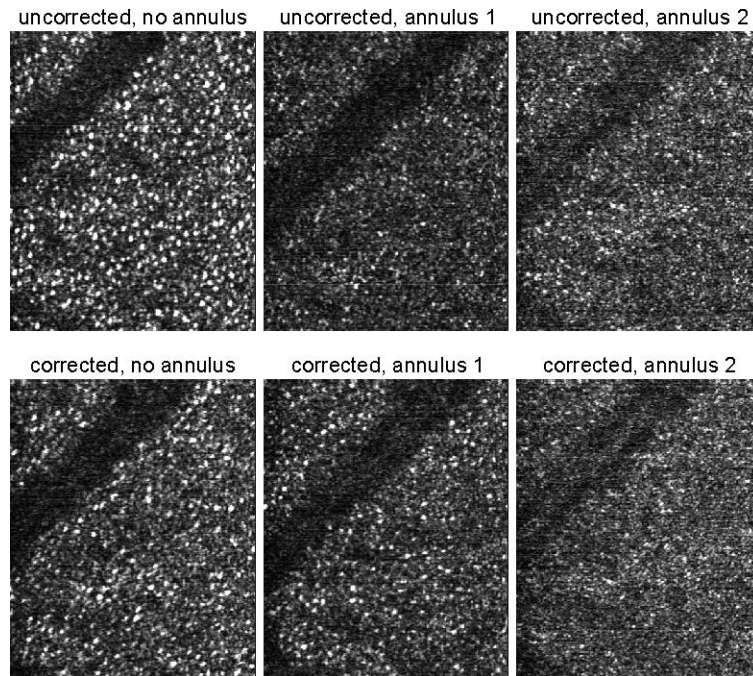


Fig. 4. Superior parafovea retina at 10° viewing angle. Image size is 230 μm × 280 μm. Upper row shows images recorded without wavefront correction (only Badal defocus correction) without an annulus ([Media 1](#)), with annulus 1 ([Media 2](#)), and with annulus 2 ([Media 3](#)). The lower row shows images recorded after wavefront correction with the deformable mirror without an annulus ([Media 4](#)), with annulus 1 ([Media 5](#)), and with annulus 2 ([Media 6](#)). Average image brightness is 75/255, 51/255, and 73/255 without and 67/255, 60/255, and 70/255 with wavefront correction.

obliquely incident light contributes at focus (with the depth-of-focus slightly increased) and rays beyond the cone acceptance angle (NA_{cone}) will couple less. As can be seen for annulus 1 in Fig. 4, the cone visibility improves slightly with correction. It is likely that this improvement stems from the correction of the wavefront so that more rays are incident within the acceptance angle of the cones with a reduced inclination of the incident wavefront [12]. That only few cones are identifiable with annulus 2 suggests that most of the incident light is contained outside of their acceptance angle which may be estimated to be on the order of $\sim 3^\circ$ ($NA_{cone} \approx 0.06$). Finally, some flickering of the cones may be appreciated in the videos that may be a consequence of interferences or reflective changes as well as changes in the coupling efficiency between the incident light and the cones for each raster scan [14].

3.2 Superior parafovea retina at 5 degrees

An example of imaging slightly smaller but more densely packed cones is shown in Fig. 5 and associated videos for the superior parafovea retina at 5° viewing angle. Here, the wavefront-corrected beam couples better to cones than the uncorrected beam suggesting a better match of the spot size (see Table 1) to the cone waveguide modes. The small 1 mm obstruction improves the apparent image quality whereas a larger central obstruction reduces the coupling and the visibility of the cones. Increased central stoppage reduces the coupling of light to the cones and the vessels become brighter with the 2 and 3 mm annuli whereas for annulus 4 the image approaches the noise level.

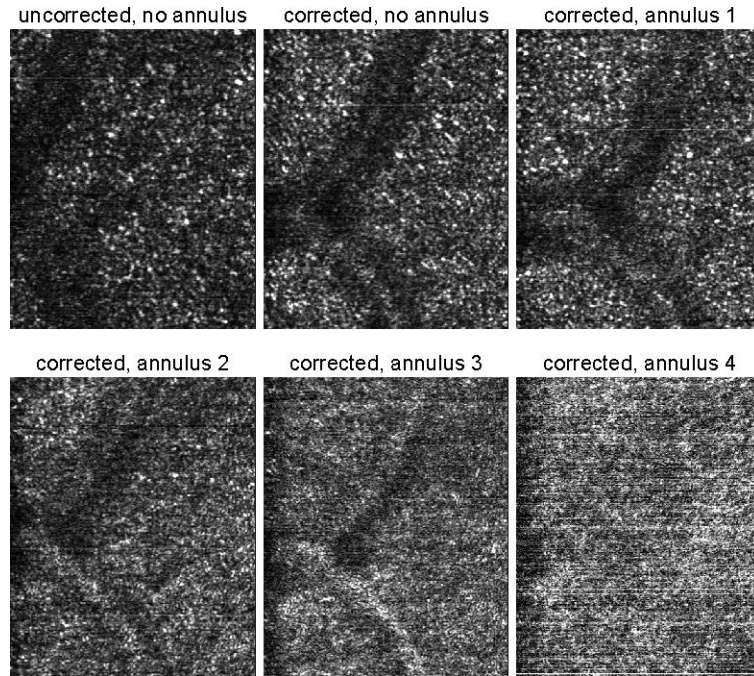


Fig. 5. Superior parafovea retina at 5° viewing angle. Image size is $230 \mu\text{m} \times 280 \mu\text{m}$. Image videos have been recorded as follows: without an annulus and without deformable mirror wavefront correction ([Media 7](#)), without an annulus but with deformable mirror wavefront correction ([Media 8](#)), with annulus 1 ([Media 9](#)), with annulus 2 ([Media 10](#)), with annulus 3 ([Media 11](#)), and with annulus 4 ([Media 12](#)). Average image brightness is 49/255, 63/255, 69/255, 73/255, 85/255, and 101/255 respectively.

3.3 Temporal parafovea retina at 2 degrees

An example of imaging yet smaller cones is shown in Fig. 6 and associated videos obtained for the temporal parafovea retina at 2° . Cones are smaller and appear bright only in a region of the images possibly because of a gradient in cone density and size (the fovea is located

beyond the left margin of the images). The best visibility is obtained with annulus 2 as best appreciated from the videos and indicating that the scanning spot size is better matched to the imaged cones in fair agreement with the expectations based on Table 1. It is important to note that the chosen pinhole size may limit the actual image resolution attainable but not the overall visibility or image brightness as determined by the coupling strength.

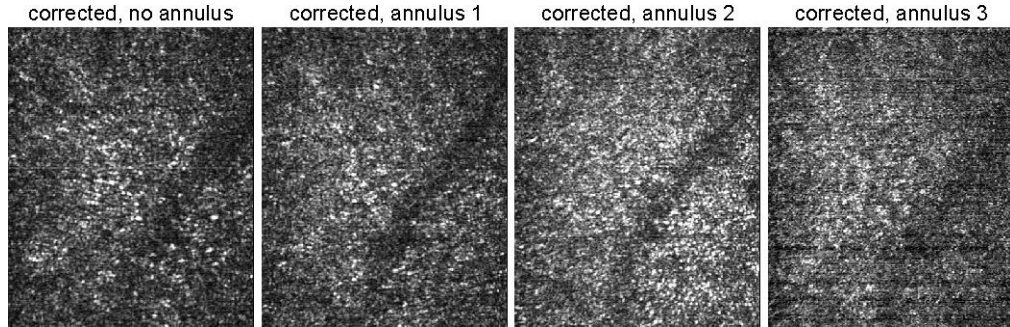


Fig. 6. Temporal parafovea retina at 2° viewing angle. Image size is 230 $\mu\text{m} \times 280 \mu\text{m}$. Image videos have been recorded as follows: With wavefront correction and without annulus ([Media 13](#)), with annulus 1 ([Media 14](#)), with annulus 2 ([Media 15](#)), and with annulus 3 ([Media 16](#)). Average image brightness is 75/255, 80/255, 106/255, and 89/255 respectively.

3.4 Fovea centralis

The main interest but also challenge for the proposed annular illumination scheme is to access and image the foveal region. The 5 mm outer beam diameter is obviously a limit of the constructed system but conceptually the same technique may be applied to other scanning retinal imaging instrumentation where an even larger entrance pupil is being successfully used [5–7]. Figure 7 (and associated videos) shows images recorded at the fovea centralis by means of the aforementioned 75 μm pinhole and may therefore not fully resolve the individual foveal cones. Indeed, the pinhole size matters directly since the images (like other confocal techniques) ultimately suffer from a convolution with the projected pinhole image [14].

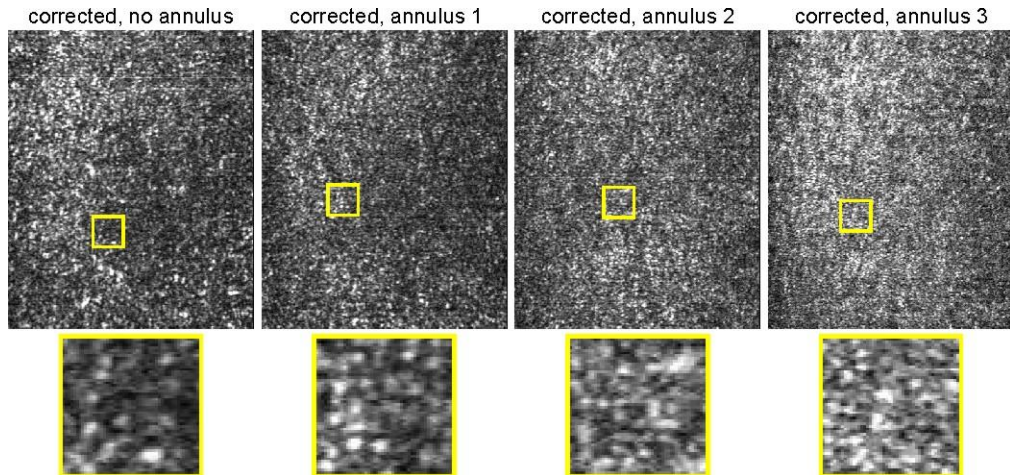


Fig. 7. Small-area fovea-centralis imaging all obtained with wavefront correction. Image size is 230 $\mu\text{m} \times 280 \mu\text{m}$. Videos have been recorded as follows: Without an annulus ([Media 17](#)), with annulus 1 ([Media 18](#)), with annulus 2 ([Media 19](#)), and with annulus 3 ([Media 20](#)). Average image brightness is 94/255, 87/255, 101/255 and 117/255 respectively. Selected magnified regions are shown below the images from which the reduced spot size with annular apertures may be appreciated.

Imaging with a smaller 50 μm pinhole (equal to 4.1 μm if projected onto the retina) has also been carried out but had lower signal and is not shown here. Absorption by the macular pigment can be ruled out at the wavelength used although melanin could play a minor role [38]. The highlighted yellow squares are zoomed-in regions to better visualize the reduction in the PSF (similar to Fig. 3) that is apparent despite of not having resolved reliably the individual foveal cones. Some bright dots tend to appear repeatedly in the fovea region that may be highly reflective cones (although not fully resolved) convolved with the projected pinhole. Similar bright dots have been reported by others for the fovea region in cases of waning resolution [6]. Similar to Fig. 6, the best brightness appears to be for annulus 2 (or possibly 3) suggesting an increased coupling. The resolution is not easily judged; however, as the overlapping cones within the area of the pinhole as well as the diffracted light outside of the Airy disc hampers the attempt at resolving the individual cones. The cones become distinguishable towards the edges of the recorded images

4. Discussion

Large parafovea cones have been resolved using wavefront-corrected SLO imaging where an annulus has been found to reduce the contrast as a result of a reduced light coupling within the acceptance angle of the cones. With the annulus a smaller spot size of the scanning beam has been obtained and this has proven useful to image cones at 2 degrees from the fovea for a 5 mm incident beam. At the fovea centralis some improvement has been obtained but the potential of the smaller spot size has still not been fully exploited. To summarize the observed contrast improvements with an annulus the average image brightness has been plotted in Fig. 8 for the different cases. The problem of noise for narrow annuli becomes apparent and is a consequence of the resulting power reduction in the reduced Airy disc.

A complication for the realization of the annular illumination has been found to be the influence of remnant aberrations across the pupil plane that may challenge its operation and the related size-reduction of the PSF also if applied with even larger entrance pupils. To estimate its impact, simulations with typical remnant aberrations (as determined by the Hartmann-Shack wavefront sensor in the SLO) have been carried out with the results shown in Fig. 9. The corrected wavefront corresponds to a remnant RMS aberration of approximately $\lambda/4$. This is still somewhat large but a consequence of fluctuations in the closed-loop wavefront correction used immediately before the image acquisition. The PSF and Strehl ratio obtained for a 3 and 4 mm inner-diameter annulus show clearly why their full potential does not appear clearly in the recorded images.

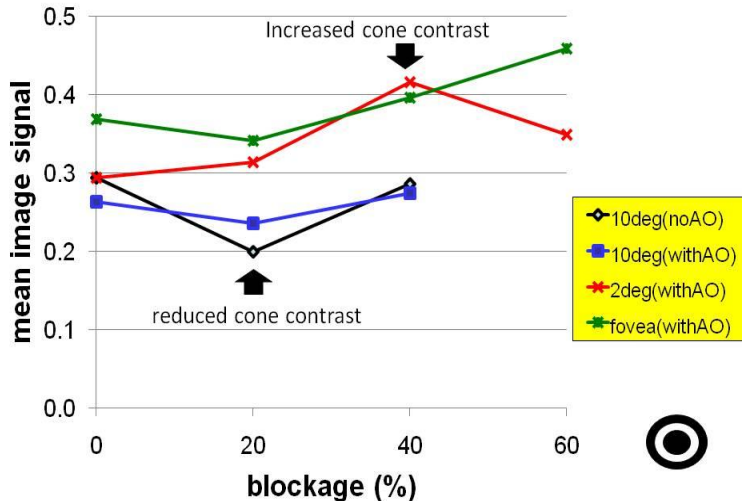


Fig. 8. Normalized averaged image brightness, $\langle \text{signal} \rangle / 255$, for different cases considered as a function of beam blockage $d_{\text{stop}}/d_{\text{pupil}}$.

Numerical estimates when down-scaling the aberration shown in Fig. 9 confirm that an RMS of less than $\lambda/10$ is needed to obtain Strehl intensity ratios on the order of 0.80 or higher as required for a more satisfactory (close to diffraction-limited) correction. We obtained this level of correction with an artificial eye (Fig. 3) but not for the eye of the subject studied.

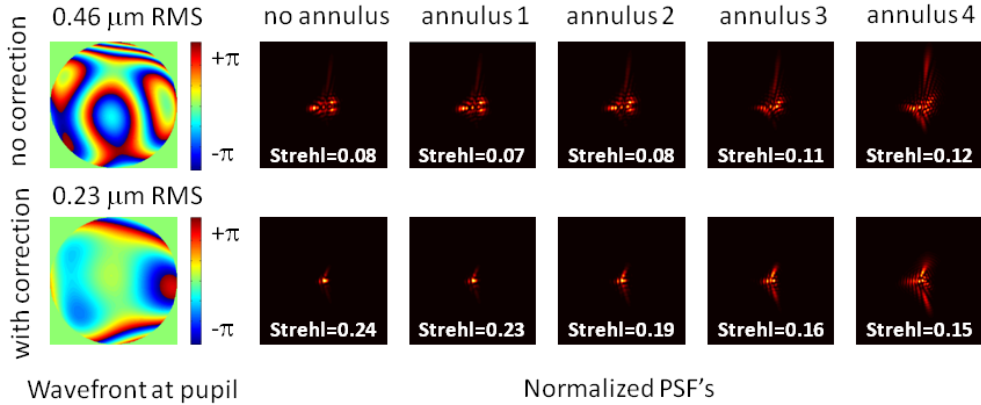


Fig. 9. Numerical estimate of the PSF with remnant aberrations as recorded by the Hartmann-Shack wavefront sensor (left) for the subject's eye in the SLO setup. The corresponding PSF's have been analyzed in the absence of the annulus and with the 1 to 4 mm central beam stop. The results have been obtained without (top) and with (bottom) wavefront correction. The calculated Strehl intensity ratios are also shown for each PSF. The wavefront has been measured, corrected, and analyzed including up to 4th-order Zernike polynomials.

Aberrations or indeed positioning inaccuracies of the central obstruction, as well as the limited stroke and accuracy of the deformable mirror used, may complicate the general applicability of the annular illumination approach for spot size reduction with an SLO. A mirror with a larger stroke in combination with the actual deformable mirror may be used to reduce the amount of remnant aberrations into a range where the full potential of the annular illumination can be utilized. Indeed, Strehl ratios above 0.8 have been reported in the literature with the use of broadband illumination [39]. The quality of wavefront correction obtained in this study is not uncommon [4] in particular when considering that the potential of adaptive optics has not been fully exploited in closed-loop correction during image acquisition with our system.

5. Conclusions

The use of an annular incident beam has been shown to reduce the probing light spot of the SLO beyond the limit of the unobstructed pupil size as directly confirmed with an artificial eye. This has been used for photoreceptor imaging both for the parafovea and fovea regions and connected to photoreceptor waveguide light coupling. A further optimization of the approach and, in particular, a reduction of the remnant aberrations is expected to lead to better resolving power with promise for imaging of individual cones at the fovea centralis. Focal control of light in terms of both amplitude and phase as suggested in this work and in a previous theoretical work [12] may possibly prove of interest for single-cone visual activation [36,40] or retina micro-surgery. The implemented central obstruction leads to an unwanted loss of light power and therefore other beam-shaping techniques including holograms or axicons may preferably be used to generate the annular illumination. Concurrent work on a retinal simulator [41] can be used to test related concepts, and may lead to new steps of relevance in relation to retinal implants for patients with reduced vision or blindness [42]. Indeed, a reduced impact of intraocular scattering is perchance the most important visual benefit of photoreceptor waveguiding.

Acknowledgments

This research has been supported by Enterprise Ireland PC/2008/0125 and Science Foundation Ireland grants 07/SK/B1239a and 08/IN.1/B2053. Clinical support by Prof. Colm O'Brien is also gratefully acknowledged.